Analyst

ROYAL SOCIETY OF CHEMISTRY

PAPER

View Article Online
View Journal | View Issue

Cite this: *Analyst*, 2022, **147**, 5680

Glucose oxidase-encapsulated liposomes for amplified autofluorescence-free immunoassay of a prostate-specific antigen with photoluminescence of $CePO_4$:Tb nanocrystals†

Xiwen Jiang,‡[a] Cuiyuan Pan,‡[a] Qiaowen Wang,‡[a] Zipeng Yin,‡[b] Xiao Han*[a] and Dianping Tang*[a,b]

Lanthanide-doped inorganic nanocrystals have attracted extensive attention due to their long luminescence lifetime and large Stokes shift. In this work, an immunosensing platform based on $CePO_4$:Tb (CPOT) was successfully constructed, which could avoid the autofluorescence interference of complex biological matrices. Specifically, CPOT was synthesized by a solvothermal method, which exhibited H_2O_2-responsive luminescence behavior. Taking advantage of this feature, an autofluorescence-free immunosensor with CPOT as the probe and H_2O_2 as the quencher was developed to detect prostate-specific antigen (PSA). Functionalized liposomes were used to encapsulate glucose oxidase (GOD) and labeled on detection antibodies to improve the sensitivity of the probe. Under the proven optimal experimental conditions, the developed autofluorescence-free immunosensor exhibited a linear luminescence response to the logarithm of PSA concentration (0.005–25 ng mL^{-1}) with a limit of detection (LOD) of 3.25 pg mL^{-1}. The performance shows that the autofluorescence-free immunosensor based on this strategy opens up a new field of vision for clinical PSA detection.

Received 14th October 2022,
Accepted 1st November 2022

DOI: 10.1039/d2an01689c

rsc.li/analyst

Introduction

Monitoring the concentration level of tumor markers in human blood or other samples is one of the important means for the early diagnosis of tumors.[1,2] Fluorescent nanoprobes, as a powerful detection technology with high sensitivity, high efficiency, and visualization, have been widely used in the detection of tumor markers in previous studies.[3–5] So far, a variety of photoluminescent materials have been used to construct fluorescent nanoprobes for food safety analysis, environmental monitoring, and disease diagnosis, such as metal–organic frameworks (MOFs),[6,7] semiconductor quantum dots,[8,9] organic fluorescent small molecules,[10,11] polymers,[12,13] and noble metal nanoclusters.[14] However, the inability to overcome the problems of complex sample autofluorescence and excitation scattered light interference is a practical problem that limits the application of traditional fluorescent nanoprobes in clinical diagnosis.[3,15]

Some trivalent lanthanide (Ln^{3+}) doped inorganic nanoparticles (NPs) possess fascinating optical properties, such as strong stability, high photoluminescence efficiency, a large Stokes shift, and a long luminescence lifetime, which bring hope to avoid the shortcomings of traditional fluorescent nanoprobes.[16–18] The green luminescence of Tb^{3+} is typical long-lived photoluminescence, generally above the millisecond level, which can be clearly distinguished from the autofluorescence in complex biological matrices.[19,20] Currently, most of the autofluorescence-free biosensors constructed from Tb^{3+} doped inorganic nanoparticles are based on the time-resolved fluorescence resonance energy transfer principle.[21,22] Niazi and colleagues[23] reported a time-resolved fluorescence sensor based on multicolor-emissive nanoparticles doped with lanthanide ions (Dy^{3+}, Tb^{3+}, Eu^{3+}) for the simultaneous detection of zearalenone (ZEN), trichothecenes A (T-2), and aflatoxin B_1 (AFB_1). Wang's group[24] developed a paper-based time-resolved fluorescence sensing platform based on a double Ln^{3+}-doped complex (Tb/DPA@SiO_2-Eu/GMP) for the sensitive and accurate detection of anthrax biomarkers (pyridine dicarboxylic acid). Despite many advances in this field, the application of Tb^{3+} doped inorganic nanomaterials with stimuli-responsive luminescence is more conducive to the introduc-

[a]*College of Biological Science and Engineering, Fuzhou University, Fuzhou 350108, P.R. China. E-mail: hanxiao@fzu.edu.cn*
[b]*Key Laboratory for Analytical Science of Food Safety and Biology (MOE & Fujian Province), Department of Chemistry, Fuzhou University, Fuzhou 350108, P.R. China. E-mail: dianping.tang@fzu.edu.cn*

†Electronic supplementary information (ESI) available. See DOI: https://doi.org/10.1039/d2an01689c

‡These authors contributed equally to this work.

tion of various signal amplification strategies to further improve the sensitivity in designing an autofluorescence-free biosensing platform.

In the field of biological analysis, enzymatic substrate amplification,[25,26] nucleic acid isothermal amplification techniques,[27] and functionalized nanomaterial labels[28] have been developed to amplify signals to improve the sensitivity of detection methods. Liposomes are spherical vesicles with a bilayer phospholipid structure and are widely used in drug delivery and bioanalysis due to their excellent biocompatibility, high loading, and low toxicity.[29] There are many methods for encapsulating drugs, enzymes, quantum dots, and other substances by liposomes.[30–32] Typically, when applied to biological analysis, functionalized liposomes are used in combination with special biorecognition units such as DNA and antibodies to serve as nano-containers that are quantitatively related to the concentration of the target.[33–35] Upon external stimulation, these containers release large amounts of signaling components, thereby amplifying the signal. Inspired by this, we are committed to introducing this signal amplification technique for the construction of stimuli-responsive autofluorescence-free biosensors to further improve their sensitivity.

As a marker of prostate cancer, accurate and rapid detection of prostate-specific antigen (PSA) is of great significance in cancer screening. In this work, we successfully synthesized $CePO_4$:Tb (CPOT) nanospheres by the solvothermal method. CPOT can emit the characteristic long-lived green luminescence of Tb^{3+} after UV lamp irradiation due to the energy transfer from Ce^{3+} to Tb^{3+}. Based on the discovery that H_2O_2 can quench the green emission of CPOT, a split-type autofluorescence-free immunosensor system was constructed (Scheme 1). During the detection process, the PSA in the sample was first captured by the capture antibody loaded on the microplate and then combined with the free monoclonal detection antibody to form a sandwich-type immune complex. Subsequently, the glucose oxidase (GOD) was released from the liposomes labeled with the monoclonal antibody under the action of Triton X-100 to catalyze the glucose in the substrate to generate H_2O_2. In the next step, the bioreaction product was mixed with CPOT to quench the latter's luminescence, enabling sensitive detection of PSA. The highly sensitive and accurate performance of this autofluorescence-free immunosensor under the optimal conditions demonstrates its feasibility in practical clinical applications.

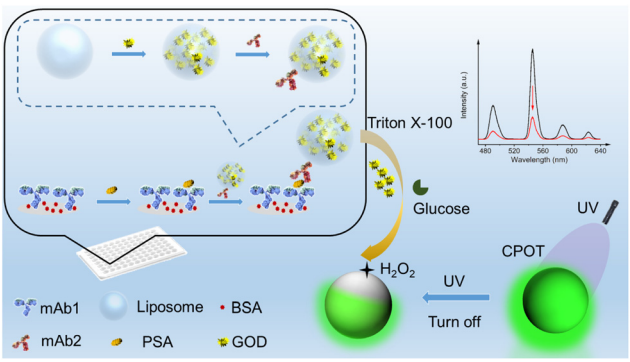

Scheme 1 Schematic illustration of the autofluorescence-free immunosensor for the detection of prostate-specific antigen (PSA).

Experimental section

Preparation of CPOT nanospheres

CPOT was synthesized by the solvothermal method.[36,37] Firstly, 25 mL of $CeNO_3$ solution (0.2 M), 25 mL of $TbNO_3$ solution (0.2 M), and 50 mL of citric acid solution (0.2 M) were prepared. Subsequently, $CeNO_3$ and $TbNO_3$ pre-formulations were added to 30 mL of ethylene glycol (the specific ratio of Ce^{3+} and Tb^{3+} was adjusted according to specific needs, and the total amount was 0.15 mmol), and then 750 μL of citric acid (2 M) pre-formulation was injected to form a complex of lanthanide and citric acid. Thereafter, 300 μL of concentrated phosphoric acid was added to the aforementioned precursor solution under vigorous magnetic stirring to provide a source of PO_4^{3-} for the reaction. After that, the mixed solution was completely transferred to a 50 mL Teflon autoclave and reacted at 150 °C for 90 min. Finally, the product was collected by centrifugation, washed twice with anhydrous ethanol and twice with water, and dried at 60 °C.

Preparation of GOD-encapsulated liposomes (G-LPs)

Liposomes encapsulating GOD were prepared according to a previous work.[30,38,39] Briefly, DPPE (7.5 μmol), DPPC (45 μmol), and cholesterol (45 μmol) were added to a 25 mL round-bottom flask containing 6 mL of chloroform. After dissolving, the solvent was evaporated to dryness using a rotary evaporator under reduced pressure at 45 °C to obtain a thin lipid film. Subsequently, 2 mL of a PBS solution (0.1 M, pH 7.4) containing 2000 U of GOD was added to the above round-bottom flask and shaken for 10 min. Then, under the conditions of an ice bath, high-power ultrasound was used for 30 min. To remove the unencapsulated GOD, the emulsion was centrifuged at 13 000 rpm for 15 min and the resulting precipitate was washed three times with PBS (0.1 M, pH 7.4). The product was redispersed in 2 mL of PBS (0.1 M, pH 7.4) and the homogeneous monodisperse liposomes were screened using a polycarbonate filter (0.22 μm), and finally stored at 4 °C.

Conjugation of G-LPs with anti-PSA mAb_2 detection antibody (G-LPs-mAb_2)

Monoclonal anti-PSA detection antibody (mAb_2) was immobilized on the outer surface of G-LPs by cross-linking with glutaraldehyde. 1 mL of the previously prepared G-LPs was added to 1.5 mL of glutaraldehyde aqueous solution (2.5%) and stirred gently at 25 °C for 1.5 h. After this, excess glutaraldehyde was removed by overnight dialysis against PBS (0.1 M, pH 7.4). Subsequently, 0.5 mL of mAb_2 (1.0 mg mL^{-1}) dispersed in PBS (0.1 M, pH 7.4) was mixed with the aforementioned solution and incubated at 4 °C with gentle shaking for 1 h. To block

the excess aldehyde groups on the G-LP surface, 500 μL of 3% BSA in PBS (0.1 M, pH 7.4) was mixed with the resulting solution and incubated overnight at 4 °C. The unbound mAb_2 and BSA were removed by centrifugation at 13 000 rpm for 20 min. Finally, the obtained G-LPs-mAb_2 was redispersed in PBS (0.1 M, pH 7.4) and stored at 4 °C for further use.

Procedure for detecting PSA without autofluorescence

Test samples containing different concentrations of PSA were initially added to each well of the prepared microplate and incubated at 37 °C for 40 min. After washing the microplates with PBS buffer (0.1 M, pH 7.4) containing 0.05% Tween 20 as the washing solution, the prepared G-LPs-mAb_2 (100 μL) was injected into the wells and incubated at 37 °C for 40 min. Then, the microplate was washed again with washing solution and 50 μL of 1% Triton X-100 solution was injected into the microwell. After 15 min of incubation, the liquid containing the liposome lysate was transferred to a centrifuge tube containing an aqueous glucose solution (50 μL, 200 mM) and CPOT (100 μL, 0.6 mg mL^{-1}) and incubated for 30 min. Finally, the photoluminescence (PL) intensity of the solution at 545 nm was measured and recorded with a fluorometer in the phosphorescence mode for the determination of PSA (excitation at 274 nm; the slit widths for both excitation and emission were set to 5.0 nm; the response time was set to 0.004 s).

Results and discussion

Detailed characterization of CPOT nanospheres

Tb-doped $CePO_4$ was obtained by the solvothermal method. Fig. 1A shows that the prepared CPOT particles presented an irregular spherical state with a diameter between 600 and 1000 nm in the transmission electron microscopy (TEM) image, which was similar to the work of Nunez *et al.*[36] In the synthesis process, Ce^{3+} and Tb^{3+} in the solution first reacted with citrate at room temperature to form a stable complex. After the introduction of PO_4^{3-}, the aforementioned complexes slowly released Ce^{3+} and Tb^{3+} to nucleate with PO_4^{3-}. In the solvent system of ethylene glycol, which has a high viscosity and certain complexing ability, small particles adsorbed with ethylene glycol molecules gathered orderly and slowly formed irregular spherical particles. The XRD pattern (Fig. 1B) of CPOT was in perfect agreement with the standard card (JCPDS no. 32-0199) of monoclinic $CePO_4$. The stronger diffraction peaks appeared at 2θ values of 20.9°, 26.9°, 28.7°, 31.0°, 34.2°, 36.7°, 41.8°, 46.2°, 48.5°, and 52.3°, which were associated with the (111), (200), (120), (012), (202), (212), (311), (212), (103) and (232) crystal planes of the $CePO_4$ crystals with the monoclinic phase, respectively. At the same time, the diffraction peaks of other crystal phases (such as the hexagonal phase) of $CePO_4$ were not observed in the XRD pattern,[40–42] indicating that the obtained CPOT had a high-purity monoclinic phase and good crystallinity.

As one of the core components of the autofluorescence-free sensing platform, the luminescence performance of CPOT directly determines the pros and cons of biosensors in detection applications. The excitation (Ex) and emission (Em) spectra of CPOT were obtained in phosphorescence mode using a fluorophotometer (Fig. 1C). The excitation band of CPOT appeared in the wavelength range of 200–320 nm and the excitation peak was at 274 nm. The characteristic emission band of Tb^{3+} could be clearly observed in the emission spectrum of CPOT in the range of 470–600 nm due to the energy transfer from Ce^{3+} to Tb^{3+}. The four characteristic emission peaks located at 490 nm, 545 nm, 587 nm, and 624 nm were caused by the electronic transition of $^5D_4$–^7F_j (j: 3, 4, 5, and 6) of Tb^{3+}, respectively. Specifically, the green emission exhibited by CPOT can be attributed to the ultra-intense green emission band in the range of 530–570 nm. To achieve an efficient signal readout, all subsequent test procedures used 274 nm as the excitation wavelength and the intensity change of the strongest emission peak at 545 nm was recorded. The luminescence decay behavior of CPOT was also measured, as shown in Fig. 1D. In order to avoid the interference of matrix autofluorescence (generally the longest lifetime is 10^{-8} s), we set the response time in the test to 4 ms, which was the fastest response time of the instrument. The luminescence signal could be maintained for about 18 ms, accompanied by a sufficiently large luminescence intensity at 4 ms of CPOT with a Tb doping ratio of 12%, which means that CPOT can be used as a luminescence unit of autofluorescence-free biosensors.

The elemental compositions and valence states of CPOT were characterized by X-ray photoelectron spectroscopy (XPS). The XPS spectrum of CPOT is shown in Fig. 2A. The peak corresponding to the P 2p level appeared at a binding energy of 132.9 eV (inset in Fig. 2A). In the high-resolution XPS spectrum of O 1s (Fig. 2B), two peaks with binding energies at 530.9 eV and 532.9 eV correspond to the unbridged oxygen (P–O) and the bridged oxygen (P–O–P), respectively, while the

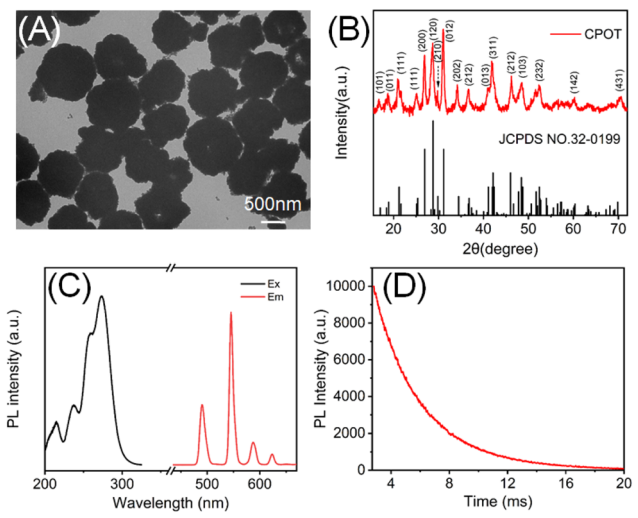

Fig. 1 (A) TEM image of CPOT; (B) powder XRD patterns of CPOT; (C) excitation (Ex) (emission at 533 nm) and emission (Em) (excitation at 254 nm) spectra of ZGOMP in phosphorescence mode; (D) luminescence decay spectrum of CPOT (excitation at 254 nm).

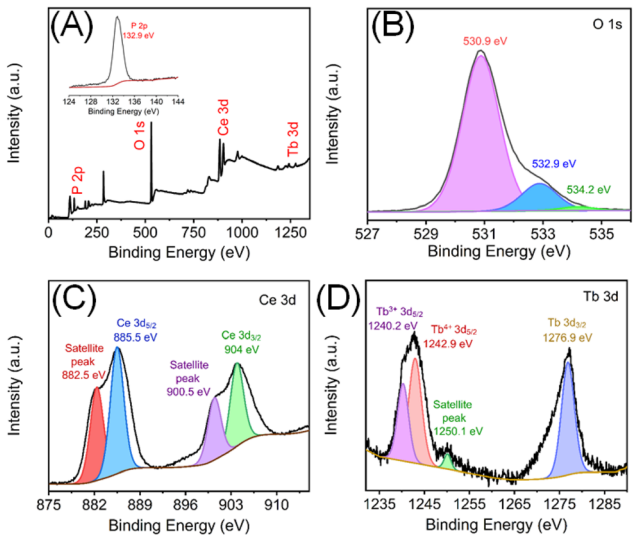

Fig. 2 (A) XPS survey spectra of CPOT (inset: high-resolution spectra of P 2p); high-resolution XPS spectra of (B) Ce 3d, (C) O 1s, and (D) Tb 3d.

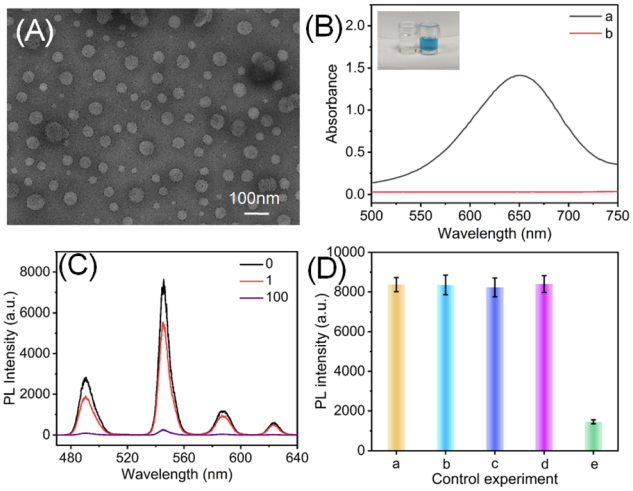

Fig. 3 (A) TEM image of liposomes; (B) UV-vis absorption spectra of line a: G-Lps (10 μL) + horseradish peroxidase (HRP, 50 U mL^{-1}, 10 μL) + glucose (10 mM, 20 μL) + 3,3′,5,5′-tetramethylbenzidine (TMB, 10 mM, 20 μL) + Triton X-100 solution (1%, 20 μL) + deionized water (100 μL) and line b: all other reagents mentioned above except for G-Lps; (C) PL intensity of CPOT after adding different concentrations of H_2O_2 (0, 1 μM, 100 μM); (D) PL intensities of (a) CPOT, (b) mAb_1 + PSA + G-Lps-mAb_2 + Triton X-100 + CPOT, (c) mAb_1 + PSA + G-Lps-mAb_2 + glucose + CPOT, (d) mAb_1 + G-Lps-mAb_2 + glucose + Triton X-100 + CPOT, and (e) mAb_1 + PSA + G-Lps-mAb_2 + glucose + Triton X-100 + CPOT (2.5 ng mL^{-1} PSA was used in this case).

peak with binding energy at 534.2 eV was attributed to the phosphorus hydroxyl group (P-OH).[43,44] These results suggested the existence of P^{5+} and O^{2-} in CPOT. The two peaks located at 885.5 eV and 904 eV in the high-resolution XPS spectrum of Ce 3d (Fig. 2C) correspond to the Ce^{3+}-3d energy levels of $3d_{5/2}$ and $3d_{3/2}$, respectively. Moreover, two satellite peaks appear at the binding energies of 882.5 eV and 900.5 eV, respectively. These results indicated the chemical state of Ce^{3+} in CPOT.[45] Besides, the characteristic peak of Tb $3d_{3/2}$ and the satellite peak appeared at 1276.9 eV and 1250.1 eV, respectively. A double peak located at 1240.2 eV and 1242.9 eV was assigned to Tb^{3+} $3d_{5/2}$ and Tb^{4+} $3d_{5/2}$, respectively,[46–48] which means that the Tb incorporated into the material existed as either Tb^{3+} or Tb^{4+} (Fig. 2D). These results indicated that Tb-doped $CePO_4$ has been successfully synthesized.

Characteristics of GOD-encapsulated liposomes (G-LPs)

The successful synthesis of liposomes as "nanocontainers" for encapsulating GOD was directly related to the realization of the signal amplification strategy. It could be observed from the TEM image that the synthesized G-Lps exhibited a relatively uniform spherical shape with a particle size of 30–90 nm (Fig. 3A). The measurement results obtained using a nanoparticle size analyzer (Fig. S1†) showed that the hydrated particle size of G-Lps exhibited a normal distribution between 33 and 220 nm, with an average of 79 nm. The reason why the two test results are not completely consistent can be attributed to the following points. On the one hand, the drying process during the preparation of electron microscope samples dehydrated the liposomes and reduced their volume; on the other hand, the hydrated particle size of the measured samples was often numerically slightly larger than their actual size.

To judge whether glucose oxidase was successfully encapsulated in liposomes and had sufficient enzymatic activity, we designed control experiments. Among them, to the experimental group was added the prepared G-Lps, horseradish peroxidase (HRP), glucose, 3,3′,5,5′-tetramethylbenzidine (TMB), and Triton X-100 solution, and the other control group was supplemented with other reagents except for G-Lps. It was clearly observed that in the presence of G-Lps, the solution was blue (Fig. 3B), while the control group was colorless. The UV-vis absorption spectrum showed that the experimental group with G-Lps had a strong absorption band at 500–700 nm, and the peak was about 652 nm, which was the characteristic absorption peak of blue TMB oxide, while the control group did not show this phenomenon. The reason is that Triton X-100 cleaved the lipid layer of G-Lps and released glucose oxidase, which can catalyze the production of H_2O_2 from glucose in the solution, while HRP can catalyze the production of $OH^{\bullet}$ from H_2O_2, thus oxidizing TMB to produce a blue product. The above results fully demonstrated that the strategy of encapsulating glucose oxidase in liposomes had been successfully realized.

Characteristics of the autofluorescence-free sensing platform based on CPOT and G-LPs

When further considering whether the designed autofluorescence-free sensing platform strategy could be successfully applied to PSA detection, we are faced with some questions that need to be verified, *e.g.*, (i) whether the luminescence of CPOT could respond to different concentrations of H_2O_2; (ii) whether the target (PSA) could perfectly trigger the biological

response and change the PL signal of CPOT. First, we designed experiments to verify whether H_2O_2 could change the PL intensity of CPOT because this was the key to the success of the entire detection strategy. We added equal volumes of different concentrations of H_2O_2 (1 μM and 100 μM) to CPOT (0.6 mg mL^{-1}), and the PL intensity of the system with a response time of 4 ms after excitation by light irradiation was recorded. As shown in Fig. 3C, compared with the blank control group without H_2O_2, the characteristic peak of Tb^{3+} emission in the experimental group was significantly reduced, which fully demonstrated that the luminescence of CPOT depends on the concentration of H_2O_2. As a reason for this phenomenon, we speculate that Ce^{3+} in CPOT may be oxidized to Ce^{4+}, which weakens the energy transfer between Ce^{3+} and Tb^{3+}, resulting in a decrease in the luminescence intensity of CPOT. A similar phenomenon was also found in the study by Lee and Perez *et al.* When encountering H_2O_2, Ce^{3+} in nano-CeO_2 could be oxidized to Ce^{4+}.[49–51]

To confirm the reliability of the designed PSA detection process, we compared the PL intensities of each system under different conditions (Fig. 3D). Obviously, in the absence of glucose, Triton X-100, or PSA (line 'b', 'c', and 'd'), the PL intensity of the system did not change significantly compared to the blank group (curve 'a'). However, the PL signal of CPOT at 545 nm decreased significantly once all necessary reagents were added according to the detection protocol (curve 'e'). The results fully demonstrated that the designed detection process was reliable enough, and the target PSA could indeed effectively trigger the biological reaction and then quenched the PL signal of CPOT. Moreover, the luminescence intensity of CPOT was unchanged at different pH values (Fig. S2†), which indicated that CPOT did not respond to another product (gluconic acid) of the enzymatic reaction. Therefore, the autofluorescence-free sensor was not sensitive to the pH of the test environment and could resist environmental interference to a certain extent.

Optimization of experimental conditions

In order to achieve the best performance of the designed sensing platform without autofluorescence, some optimization conditions were explored and finally implemented into materials synthesis and biological reactions. First, we tried to obtain CPOT with the highest luminescence intensity by exploring an optimal Tb doping ratio. The recorded PL spectra (Fig. 4A) showed that the intensities of the four characteristic emission peaks of Tb^{3+} first increased and then decreased with the doping ratio of Tb, and the Tb doping ratio of CPOT with the strongest luminescence was 12%. We speculate that the reason may be that the number of luminescent centers increases with the increase in the doping ratio of Tb. However, when the doping level reaches a certain level, concentration quenching occurs inside the CPOT. Finally, we chose the Tb doping ratio of 12% as the optimal synthetic doping ratio of CPOT.

In addition, we explored the optimal time of immune complex formation and enzymatic reactions. As shown in Fig. 4B, with the prolongation of the incubation time, the PL signal of the system gradually became weaker and the curve became flat at 40 min, indicating that the antigen–antibody reaction had been fully carried out within this time, and enough H_2O_2 was generated in the system to quench the signal of CPOT. To improve the detection efficiency, the antigen–antibody reaction time and the enzymatic reaction time in the subsequent detection were 40 min and 30 min, respectively (Fig. 4C).

Analytical performance of the CPOT-based autofluorescence-free sensing system

The detection performance of the CPOT-based H_2O_2 stimuli-responsive autofluorescence-free sensing platform was evaluated by detecting different concentrations of PSA standard samples. Under the optimal experimental conditions, the response of the PL signal of the autofluorescence-free biosensor to PSA is shown in Fig. 5A. With the increase of PSA concentration, the catalytically generated H_2O_2 in the system increased, which quenched the PL signal of CPOT. In the concentration range of 0.005–25 ng mL^{-1}, the logarithm of PSA concentration was linearly related to the attenuation degree of the PL signal (ΔF) of CPOT at 545 nm, and the linear equation was $\Delta F = 2078.4 \times \lg C_{[PSA]} - 510.6$ ($R^2 = 0.9912$, $n = 9$) with a limit of detection (LOD) of 3.25 pg mL^{-1} (Fig. 5B). Compared with other strategies (Table S1†), this autofluorescence-free biosensor based on CPOT and G-LPs is more sensitive to detecting PSA. Impressively, the wide linear range and low LOD indicated that this strategy could fully meet the needs of PSA detection in clinical applications.

It is necessary to evaluate the selective performance of the developed autofluorescence-free biosensing platform, which

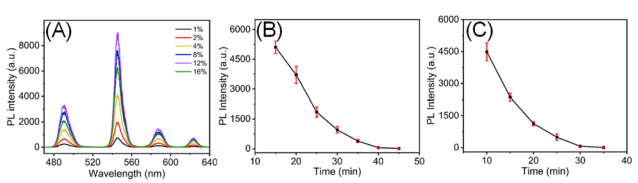

Fig. 4 Optimization of (A) Tb doping ratio, (B) antigen–antibody reaction time, and (C) enzyme catalysis time (25 ng mL^{-1} PSA was used as an example).

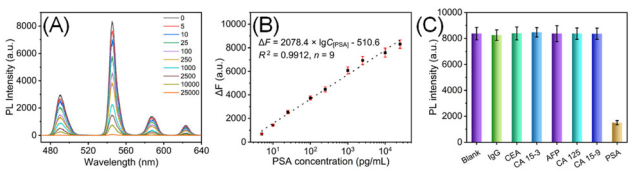

Fig. 5 (A) Luminescence response of the H_2O_2-responsive autofluorescence-free biosensor to PSA standard samples with different concentrations; (B) linear regression equation; and (C) selectivity of the H_2O_2-responsive autofluorescence-free biosensor against PSA (2.5 ng mL^{-1}), IgG (25 ng mL^{-1}), CEA (25 ng mL^{-1}), CA 15-3 (25 ng mL^{-1}), AFP (25 ng mL^{-1}), CA 125 (25 ng mL^{-1}) and CA 15-9 (25 ng mL^{-1}).

Table 1 Comparison of the results obtained using a CPOT-based autofluorescence-free biosensor and a commercial human PSA-ELISA kit

	Method; concentration (mean ± SD, ng mL^{-1}, n = 3)		
Sample no.	Autofluorescence-free sensing assay	PSA ELISA kit	t_{exp}
1	12.78 ± 1.01	13.53 ± 1.08	0.88
2	3.12 ± 0.25	2.93 ± 0.19	1.06
3	1.70 ± 0.11	1.66 ± 0.11	0.42
4	8.59 ± 0.56	8.31 ± 0.50	0.64
5	17.34 ± 1.17	18.58 ± 0.98	1.41
6	0.42 ± 0.02	0.36 ± 0.04	2.26
7	5.87 ± 0.32	5.77 ± 0.31	0.42

involved the ability of the biosensor to specifically recognize and detect PSA. We used this autofluorescence-free biosensor to detect some common biomarkers, and the results obtained are shown in Fig. 5C. When the sample contained PSA (2.5 ng mL^{-1}), the PL signal decreased significantly compared with the blank group. However, when IgG, CEA, CA 15-3, AFP, CA 125, or CA 15-9 was present in the samples (the concentrations of these biomarkers were 10-fold higher than the above PSA concentrations), the PL signal did not change significantly compared to the blank group. The above results imply that the autofluorescence-free biosensing platform has extreme specificity in monitoring PSA concentration levels and can resist the interference of other biomarkers.

Preliminary application in real samples

The practical application potential of this autofluorescence-free biosensing platform needs to be further investigated. To this end, seven real samples of human serum from the local Fujian Provincial Hospital were detected with the designed autofluorescence-free biosensor, and PSA concentrations were calculated using the obtained linear regression equation (Fig. 5B). At the same time, for comparison, the same samples were also tested with a commercial ELISA kit. The correlation between the two groups of data was evaluated by the classical t-test statistical analysis method to judge the reliability of the two detection methods. As shown in Table 1, all t_{exp} values are lower than 2.78 ($t_{crit}[0.05,4] = 2.78$), which proves that the two groups of data obtained are not significantly different at the 95% confidence level. It can also be interpreted that both methods are reliable enough. The above results fully demonstrate that the developed PSA detection method has good accuracy in the case of actual samples and is very promising in practical applications.

Conclusions

In summary, we have demonstrated a sensitive and feasible H_2O_2-responsive autofluorescence-free biosensor based on CPOT for the quantitative determination of PSA. As a "nano container" carrying the signal amplification function, the liposome is labeled on the detection antibody to realize the signal amplification function. Under specific stimuli, the "nanocontainer" releases GOD to catalyze the generation of H_2O_2 from glucose, thereby reducing or quenching the PL signal of CPOT. Compared with traditional fluorescent biosensors, this biosensing platform based on long-lived luminescent nanomaterials can successfully avoid the interference of matrix autofluorescence and excitation of scattered light and exhibits high sensitivity and accuracy. This work provides a good strategic model for the study of stimuli-responsive autofluorescence-free biosensors.

Conflicts of interest

There are no conflicts to declare.

Acknowledgements

The authors acknowledge the financial support from the National Natural Science Foundation of China (grant no.: 21874022 and 22274022).

References

1 K. Zhang, S. Lv, M. Lu and D. Tang, *Biosens. Bioelectron.*, 2018, **117**, 590–596.
2 Z. Yu, G. Cai, X. Liu and D. Tang, *ACS Appl. Mater. Interfaces*, 2020, **12**, 40133–40140.
3 Z. Farka, T. Juriik, D. Kovaar, L. Trnkova and P. Sklaadal, *Chem. Rev.*, 2017, **117**, 9973–10042.
4 C. Fang, C. Chou, Y. Yang, T. Wei-Kai, Y. Wang and Y. Chan, *Anal. Chem.*, 2018, **90**, 2134–2140.
5 R. Ranjan, E. Esimbekova and V. Kratasyuk, *Biosens. Bioelectron.*, 2017, **87**, 918–930.
6 B. Mohan, S. Kumar, H. Xi, S. Ma, Z. Tao, T. Xing, H. You, Y. Zhang and P. Ren, *Biosens. Bioelectron.*, 2022, **197**, 113738.
7 J. Dong, D. Zhao, Y. Lu and W. Sun, *J. Mater. Chem. A*, 2019, **7**, 22744–22767.
8 C. Ji, Y. Zhou, R. Leblanc and Z. Peng, *ACS Sens.*, 2020, **5**, 2724–2741.
9 F. Wang, L. Wang, J. Xu, K. Huang and X. Wu, *Analyst*, 2021, **146**, 4418–4435.
10 G. Niu, R. Zhang, X. Shi, H. Park, S. Xie, R. Kwok, J. Lam and B. Tang, *TrAC, Trends Anal. Chem.*, 2020, **123**, 115769.
11 D. Cao, Z. Liu, P. Verwilst, S. Koo, P. Jangili, J. Kim and W. Lin, *Chem. Rev.*, 2019, **119**, 11550–11550.
12 Z. Zhang, Y. Wu, S. He, Y. Xu, G. Li and B. Ye, *Anal. Chim. Acta*, 2018, **1014**, 85–90.
13 J. Yu and C. Zhang, *J. Mater. Chem. C*, 2020, **8**, 16463–16469.
14 D. Li, G. Wang and X. Mei, *Analyst*, 2020, **145**, 7150–7161.
15 D. Tu, L. Liu, Q. Ju, Y. Liu, H. Zhu, R. Li and X. Chen, *Angew. Chem., Int. Ed.*, 2011, **50**, 6306–6310.
16 K. Zhang, Q. Yu, H. Wei, S. Liu, Q. Zhao and W. Huang, *Chem. Rev.*, 2018, **118**, 1770–1839.

17 Y. Liu, S. Zhou, Z. Zhuo, R. Li, Z. Chen, M. Hong and X. Chen, *Chem. Sci.*, 2016, **7**, 5013–5019.
18 H. Zeng, F. Liu, Z. Peng, K. Yu, L. Rong, Y. Wang, P. Wu, R. Liang and J. Qiu, *ACS Appl. Nano Mater.*, 2020, **3**, 2336–2345.
19 W. Di, X. Zhao, Z. Nie, X. Wang, S. Lu, H. Zhao and X. Ren, *J. Lumin.*, 2010, **130**, 728–732.
20 M. Skwierczynska, M. Runowski, P. Kulpinski and S. Lis, *Carbohydr. Polym.*, 2019, **206**, 742–748.
21 S. Niazi, I. Khan, L. Yan, M. Khan, A. Mohsin, N. Duan, S. Wu and Z. Wang, *Anal. Bioanal. Chem.*, 2019, **411**, 1453–1465.
22 Q. Ju, D. Tu, Y. Liu, R. Li, H. Zhu, J. Chen, Z. Chen, M. Huang and X. Chen, *J. Am. Chem. Soc.*, 2012, **134**, 1323–1330.
23 S. Niazi, I. Khan, Y. Yu, I. Pasha, M. Shoaib, A. Mohsin, B. Mushtaq, W. Akhtar and Z. Wang, *Mikrochim. Acta*, 2019, **186**, 575.
24 Q. Wang, S. Xue, Z. Chen, S. Ma, S. Zhang, G. Shi and M. Zhang, *Biosens. Bioelectron.*, 2017, **94**, 388–393.
25 R. Zeng, Z. Luo, L. Zhang and D. Tang, *Anal. Chem.*, 2018, **90**, 12299–12306.
26 R. Zeng, W. Wang, M. Chen, Q. Wan, C. Wang, D. Knopp and D. Tang, *Nano Energy*, 2021, **82**, 105711.
27 R. Zeng, Z. Luo, L. Su, L. Zhang, D. Tang, R. Niessner and D. Knopp, *Anal. Chem.*, 2019, **91**, 2447–2454.
28 X. Han, H. Zhang and J. Zheng, *Anal. Chem.*, 2019, **91**, 2224–2230.
29 Q. Liu and B. Boyd, *Analyst*, 2013, **138**, 391–409.
30 G. Cai, Z. Yu, P. Tong and D. Tang, *Nanoscale*, 2019, **11**, 15659–15667.
31 G. Liu, J. Ling, H. Xie and J. Li, *Sens. Actuators, B*, 2022, **355**, 131263.
32 X. Liang, C. Gao, L. Cui, S. Wang, J. Wang and Z. Dai, *Adv. Mater.*, 2017, **29**, 1703135.
33 R. Zeng, L. Zhang, Z. Luo and D. Tang, *Anal. Chem.*, 2019, **91**, 7835–7841.
34 H. Gong, Y. Wu, R. Zeng, Y. Zeng, X. Liu and D. Tang, *Chem. Commun.*, 2021, **57**, 8977–8980.
35 R. Ren, G. Cai, Z. Yu and D. Tang, *Sens. Actuators, B*, 2018, **265**, 174–181.
36 N. Nunez, S. Liviano and M. Ocana, *J. Colloid Interface Sci.*, 2010, **349**, 484–491.
37 A. Wu, H. Bai, J. Bao, K. Yang, L. Feng, Y. Ma, Y. Qiao, W. Li, Y. Liu and X. Zhu, *RSC Adv.*, 2018, **8**, 35813–35818.
38 J. Zhuang, B. Han, W. Liu, J. Zhou, K. Liu, D. Yang and D. Tang, *Biosens. Bioelectron.*, 2018, **99**, 230–236.
39 J. Xu, Y. Li, H. Gong, Z. Yu, J. Zhang, Q. Wei and D. Tang, *ACS Appl. Nano Mater.*, 2021, **4**, 10943–10951.
40 J. Bao, R. Yu, J. Zhang, D. Wang, J. Deng, J. Chen and X. Xing, *Scr. Mater.*, 2010, **62**, 133–136.
41 C. Cheng, F. Chen, H. Yi and G. Lai, *Mater. Lett.*, 2021, **284**, 129032.
42 F. Li, M. Wang, C. Mi, K. Yi and S. Xu, *J. Alloys Compd.*, 2009, **486**, L37–L39.
43 T. Yi, Y. Zhang, J. Li and X. Yang, *Chin. J. Catal.*, 2016, **37**, 300–307.
44 Y. Zeng, Y. Wang, S. Zhang, Q. Zhong, W. Rong and X. Li, *J. Colloid Interface Sci.*, 2018, **524**, 8–15.
45 K. Yang, Y. Li, Y. Ma, L. Feng, A. Wu, Y. Qiao, J. Bao, W. Li, X. Zhu and R. Yu, *CrystEngComm*, 2018, **20**, 6351–6357.
46 M. Colomer, E. Rodríguez, M. Morán-Pedroso, F. Vattier and A. de Andrés, *J. Alloys Compd.*, 2021, **853**, 156973.
47 M. Balaguer, C. Yoo, H. M. Bouwmeester and J. Serra, *J. Mater. Chem. A*, 2013, **1**, 10234–10242.
48 Y. Sohn, *Ceram. Int.*, 2014, **40**, 13803–13811.
49 S. Lee, W. Song, M. Cho, H. Puppala, P. Nguyen, H. Zhu, L. Segatori and V. Colvin, *ACS Nano*, 2013, **7**, 9693–9703.
50 J. Perez, A. Asati, S. Nath and C. Kaittanis, *Small*, 2008, **4**, 552–556.
51 S. Lee, H. Zhu, E. Contreras, A. Prakash, H. Puppala and V. Colvin, *Chem. Mater.*, 2012, **24**, 424–432.